



Schottky switch derived by metallic W_5N_4 | catalyst junction: Switch-on to enhance catalytic activity and durability in water splitting reaction

Selvaraj Seenivasan^{a,b}, Hyeonae Im^c, Taewaeon Lim^{a,b}, Jeong Woo Han^c, Junhyeok Seo^{a,b,*}

^a Department of Chemistry, Gwangju Institute of Science and Technology, Gwangju 61005, Republic of Korea

^b Research Center for Innovative Energy and Carbon Optimized Synthesis for Chemicals (Inn-ECOSysChem), Gwangju Institute of Science and Technology, Gwangju 61005, Republic of Korea

^c Department of Chemical Engineering, Pohang University of Science and Technology (POSTECH), Pohang, Gyeongbuk 37673, Republic of Korea

ARTICLE INFO

Keywords:

Schottky junction
Metallic electrodes
Tungsten nitride
Water splitting
Seawater electrolysis

ABSTRACT

In water splitting reactions, (oxy)hydroxide catalysts generated in situ have been commonly suggested as real-time active species; however, their poor electrical conductance severely restricts catalytic reactivity. We here demonstrate that a classical unipolar Schottky junction electrode can nullify non-conductive lamination of poor-conductive catalysts; we use a water splitting reaction in our model study. Nickel-tungsten nitride (Ni- W_5N_4) alloy catalyzed HER, recording 10 mA/cm² at overpotential of 11 mV (without iR compensation). The Ni- W_5N_4 |NiFeOOH forms a rectifying Schottky junction to accelerate electron-flow across the junction; this results in excellent OER activity. The forward biased Ni- W_5N_4 |NiFeOOH Schottky junction yielded 10 mA/cm² at overpotential of 181 mV (without iR compensation). The remarkable catalytic activity is attributed to the fundamental Schottky junction rather than to electrode|electrolyte interface. Moreover, demonstration of overall seawater splitting using a full cell setup showed high current density of 100 mA/cm² at only 230 mV overpotential with outstanding durability.

1. Introduction

Commercial production of green H_2 is a promising solution to current energy issues and threats of climate change [1,2]. Electrochemical water splitting has gained great attention due to its simple operation, easy scale-up, high purity of products, zero-carbon emission, and cheap resource, i.e., sea water [3–5]. A bottleneck in establishing H_2 production by electrochemical water splitting is the preparation method for robust catalysts having adequate performance and durability under industrial operating conditions [6]. Proton adsorption on the electrode surface is a critical step; metallic alloys with a large work function can, due to their proton-adsorbing ability, produce adequate catalysts for water splitting [7]. However, research over a decade has revealed that real-time active species form as (oxy)hydroxide phases via a reconstruction process in alkaline oxygen evolution conditions [8–10]. However, the low electrical conductivity of (oxy)hydroxides due to their semiconducting nature makes their commercialization difficult. Identifying electrode surface composition is indispensable to elucidating catalytic reactions. Augmentation of surface-active sites has been found to be effective at improving catalytic performance regardless of electrode

material or electrochemical reaction pathway [11]. Hetero-structures, such as a typical core-shell architecture, exhibit high-performance in various electrochemical reactions; however, the dominance of the electrical double layer (EDL) and other ‘synergistic’ modifications produce a situation involving obscure electrochemistry [12]. Electrochemical phenomena at the solid-solid interface must be understood because the junction determines the flow of electrons.

Recently, Schottky junctions (SJ), defined originally in classical electricity theory, have been implemented in electrochemical water splitting reactions [13,14]. Common electrical circuits use metal|semiconductor in contact to prevent (off-mode) or accelerate (on-mode) free electron-flow across the junction by switching the operation according to the type of semiconductor or direction of an applied external bias. Two critical parameters of Schottky barrier height (ϕ_{SBH}) and built-in voltage barrier (V_{Bi}) determine flow of electrons across the junction [15]. The ϕ_{SBH} is a constant value preventing flow of electrons across the junction in ‘off-mode’; however, external modulation of V_{Bi} enables electrons to flow through the junction in ‘on-mode’. The on-mode can be used to overcome the poor electrical conductivity of oxy(hydroxide) active sites. Despite this well-known theory, demonstrations of the

* Corresponding author at: Department of Chemistry, Gwangju Institute of Science and Technology, Gwangju 61005, Republic of Korea.
E-mail address: seojh@gist.ac.kr (J. Seo).

<https://doi.org/10.1016/j.apcatb.2023.123233>

Received 5 June 2023; Received in revised form 14 August 2023; Accepted 27 August 2023

Available online 30 August 2023

0926-3373/© 2023 Elsevier B.V. All rights reserved.

concept in electrochemical water splitting are scarce and synthetic design and construction of concept-applied catalysts have rarely been seen [16–18].

Herein, as a model study, we report a proof-of-concept strategy to elucidate the electrochemistry reaction mechanism in an SJ using the oxygen evolution reaction (OER) and hydrogen evolution reaction (HER). SJ is formed at the interface of nickel-tungsten nitride alloy ($\text{Ni-W}_5\text{N}_4$) and n-type nickel iron oxyhydroxide (NiFeOOH). Quantification of the junction resistance at the metal/semiconductor interface under the operating conditions of OER and HER reveals the working mechanism, as well as providing synthetic insights to materialize SJ in electrocatalysis.

2. Experimental

2.1. Synthesis of $\text{Ni-W}_5\text{N}_4/\text{NiFeOOH}$ (NWN/NFO) electrocatalyst

2.1.1. Synthesis of NiWOH (NWOH) polyhedrons

NWOH polyhedrons were synthesized on Ni foam (NF) using a hydrothermal method. A piece of Ni foam (2×5 cm) was cleaned by ultrasonication in 1 M HCl, ethanol and deionized (DI) water (10 min for each), and dried. Precursor solution was prepared by dissolving 0.35 g of nickel nitrate and 0.30 g of ammonium paratungstate in 80 mL of DI water (Ni/W molar ratio = 9). The hydrothermal reaction was conducted at 180°C for 10 h in a Teflon-lined autoclave containing the precursor solution. Finally, NWOH obtained on Ni foam was rinsed with DI water and ethanol and then dried at 60°C for 12 h. In preparing the control samples, Ni/W molar ratio was varied from 0 to 12.

2.1.2. Synthesis of $\text{Ni-W}_5\text{N}_4$ (NWN) polyhedrons

NWOH polyhedrons were further heated in a tube furnace at 500 – 650°C for 60 min under a flowing ammonia (200 sccm) and argon (50 sccm) gas mixture at a heating rate of $5^\circ\text{C}/\text{min}$; samples were then cooled naturally to room temperature under argon gas flow (250 sccm).

2.1.3. Synthesis of $\text{Ni-W}_5\text{N}_4/\text{NiFe(O)OH}$ (NWN/NFO) polyhedrons

NiFe(O)OH (NFO) layer was fabricated on NWN polyhedrons via simple dip coating process. Precursor solution was prepared by dissolving nickel nitrate and iron nitrate (in equal molar concentrations of 0 – 0.03 g/mol) in 10 mL of dimethylformamide (DMF). NWN polyhedrons were soaked in the precursor solution for 15 min and exposed to an N_2 gas stream to remove excess precursors; they were then dried at 80°C for 4 h.

2.2. Synthesis of control samples

2.2.1. RuO_2 and Pt/C electrodes

Catalyst ink was prepared by mixing 10 mg of Pt/C or RuO_2 powder and 10 μL of Nafion in 1 mL of a water/ethanol mixture (3:1). The catalyst powder was dispersed using ultra-sonication and uniformly coated on clean NF via drop casting. The prepared electrodes were heated at 60°C for 6–8 h.

2.2.2. NiO powder

Precursor solution was prepared by dissolving 0.35 g of nickel chloride and 0.53 g of urea in 80 mL of DI water. The hydrothermal reaction was conducted at 120°C for 8 h in a Teflon-lined autoclave containing the precursor solution. The obtained powder sample were rinsed with DI and then dried at 60°C for 12 h. The dried powder sample annealed at 350°C for 2 h in atmospheric condition.

2.3. Characterization

Crystallinity of each sample was analyzed using a high-resolution X-ray diffractometer (XRD; Rigaku) equipped with a $\text{Cu K}\alpha$ radiation emitter at 9 kW using a PIXcel^{2D} detector. High-resolution X-ray

photoelectron spectroscopy (XPS; NEXSA, Thermo Fisher Scientific) with $\text{Al K}\alpha$ radiation and a 128-Channel detector were employed. The structural and morphological properties of the electrode materials were analyzed using high-resolution transmission electron microscopy (HR-TEM, Tecnai G2 F20 S-Twin) and high-resolution scanning electron microscopy (HR-SEM; Verios 5UC, Thermo Fisher Scientific) coupled with an energy-dispersive X-ray spectroscopy (EDS) analyzer (accelerating voltage of 30 kV). X-ray absorption spectra (XAS) was obtained using R-XAS (Rigaku, Japan) coupled with tungsten filament and Ge-220 crystal for analysis of extended X-ray absorption fine structure (EXAFS) region. The X-ray source was set to 10 keV and 40 mA and the Ni K edge X-ray absorption near edge structure (XANES) region were collected at room temperature in transmission mode for energy calibration and Ni foil uses as reference.

2.4. Electrochemical measurements

Electrochemical measurements were conducted using a three-electrode system with an Hg/HgO reference electrode and a graphite rod counter electrode. To minimize the capacitive current, catalytic performance of electrode samples was evaluated in 1 M KOH electrolyte at a scan rate of 2 mV/s. Using the Nernst equation, the measured potentials versus Hg/HgO were converted to potential versus a reversible hydrogen electrode (RHE). Electrochemical impedance spectroscopy measurements were conducted in 1 M KOH at frequencies ranging from 10^{-2} to 10^5 Hz. Electrochemically active surface area (ECSA) was estimated by calculating electrochemical double-layer capacitance (C_{dl}) in a non-Faradaic potential region. Cyclic voltammetry (CV) was conducted at scan rates of 5, 10, 20, 30, 40, and 50 mV/s. Plotting current density difference (ΔI) against scan rates yielded a slope of $2C_{dl}$, where $2C_{dl} = d(\Delta I)/dv$. Chronopotentiometry measurements were conducted in a two-electrode setup at a constant current density with frequent replacement of electrolyte. Amount of gas evolution during electrolysis was analyzed by gas chromatography (WE-Glassy carbon-05-00-PTFE-08.5–80, WIZMAC).

2.5. Computational details

Spin-polarized density functional theory calculations were performed using the Vienna ab initio simulation package (VASP). The Revised Perdew-Burke-Ernzerhof (RPBE) functional was selected to describe the exchange-correlation function. The plane-wave was treated with a cutoff energy of 500 eV, and convergence criteria were set to be 10^{-4} eV/atom and 0.08 eV/Å for energy and force, respectively. The W_5N_4 bulk and Ni bulk structures were optimized with $8 \times 8 \times 8$ and $5 \times 5 \times 5$ Monkhorst-Pack k-point sampling, respectively. The W_5N_4 (100) and Ni (111) slabs were modeled with 4 and 6 layers, respectively, and each slab structure had a 15 Å vacuum space in the z-axis direction and 2 bottom-fixed layers. The W_5N_4 (100), Ni (111), and $\text{W}_5\text{N}_4(100)/\text{Ni}(111)$ slabs were optimized with $4 \times 4 \times 1$, $3 \times 3 \times 1$ and $1 \times 1 \times 1$ Monkhorst-Pack k-point sampling, respectively. The activation energies of water dissociation were calculated using the climbing image NEB (Nudged Elastic Band) method. The hydrogen adsorption free energies (ΔG_H) were calculated by correcting the hydrogen adsorption energy (ΔE_H) with zero-point energy (ΔZPE) and entropy (ΔS) as.

$$\Delta G_H = \Delta E_H + \Delta ZPE - T\Delta S,$$

where T represents the room temperature. The hydrogen adsorption energies (ΔE_H) were calculated as.

$$\Delta E_H = E^*_{\text{H}} - (E^* + 0.5E_{\text{H}_2})$$

where E^* , E^*_{H} , E_{H_2} represent the total energies of bare surface, hydrogen adsorbed surface and isolated hydrogen (H_2) molecule, respectively.

3. Discussion

3.1. Synthesis and physical characterization

The X-ray diffraction (XRD) spectra of NWOH electrode materials closely matched the characteristic peaks of the $\text{Ni}_4\text{W}_6\text{O}_{21}(\text{OH})_2 \cdot 4\text{H}_2\text{O}$ structure (Fig. S1a). The WN and NWN samples showed distinct peaks at 36.3° , 46.5° , and 64.4° (Fig. 1a), corresponding to the (101), (105), and (110) lattice planes of W_5N_4 structure (JCPDS: 65–4761) [19,20]. Diffraction peaks of Ni foam were detected together in those XRD spectra (JCPDS: 04–0850). The XRD spectra of NWN samples having various Ni/W molar ratios were compared to examine the Ni alloying effects in the W_5N_4 lattice, but no peak shift was detected in the comparison (Fig. S1b). The NWN powder sample in absence of Ni foam substrate exhibited sharp metallic Ni peaks (Fig. S1c) but no other diffraction peaks assignable to Ni ion's crystalline phases. This indicates that Ni incorporation formed an alloy with W_5N_4 under nitration condition even at 550°C temperature. In addition, X-ray absorption spectroscopy was used to analyze the impact of Ni alloying with W_5N_4 . The

radial structure function around Ni was determined by the Fourier transform of EXAFS for NWN sample as shown in Fig. 1b. The dominant peak at 2.16 \AA corresponds to the Ni–Ni coordination, which indicates alloy formation in the NWN sample [21]. To verify the absence of Ni ion's crystalline phases, EXAFS of a NiO control sample was compared to that of the NWN sample. The NiO sample showed intrinsic Ni–O coordination peak at 1.62 \AA and Ni–Ni peak at 2.58 \AA , while the NWN exhibited no significant Ni–O coordination peak [22,23].

The high resolution X-ray photoelectron spectrum (XPS) of a NWN sample in the Ni 2p region exhibits a major peak at 852.68 eV , assigned to Ni^0 , and another peak at 855.13 eV for the Ni^{2+} state, along with two satellite peaks (Fig. 1c) [24]. The dominant Ni^0 peak indicates the presence of metallic Ni alloyed with W_5N_4 . The WN sample shows a small Ni^0 peak and a dominant Ni^{2+} peak, indicating that the dominant Ni^0 peak of the NWN sample is from the Ni alloy formation. The surface compositions of the electrode samples are listed in Table S2. The $\text{Ni}^0/\text{Ni}^{2+}$ atomic ratio decreased from 1.976 to 1.057 after incorporation of NFO into NWN due to electronic equilibration at the interface of NWN and NFO. High resolution XPS of the WN sample in the W 4f region

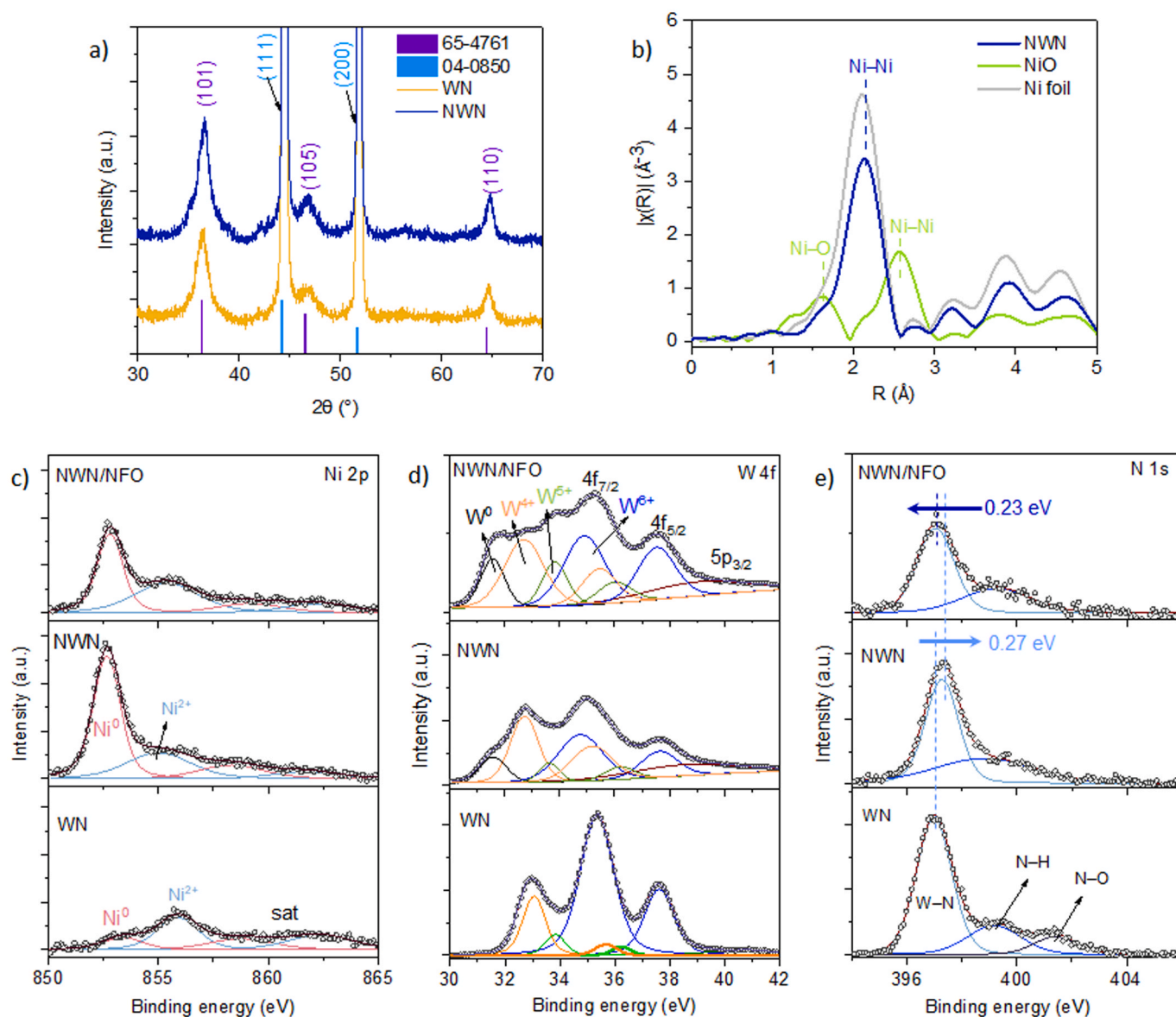


Fig. 1. a) XRD spectra of WN and NWN electrodes coated on Ni foam; b) Fourier transformed Ni K-edge EXAFS of NWN sample and NiO control sample; high resolution XPS in the region of c) Ni 2p, d) W 4f, and e) N 1s spectra of WN, NWN, and NWN/NFO samples.

showed mixed oxidation states of W^{4+} , W^{5+} , and W^{6+} , with well-fitted fragment peaks at 33.06, 33.83, and 35.36 eV, respectively (Fig. 1d) [25]. The Ni-WN alloying procedure allowed for the emergence of a W^0 peak at 31.57 eV in the NWN sample. Binding energies of the W^{6+} and W^{4+} 4 f electrons decreased by 0.40 eV and 0.42 eV, respectively, in the presence of Ni^0 . The W_5N_4 unit cell contained 0.25 W sites bound by 0.5 N sites [26]. Ni-alloying into the W_5N_4 lattice causes an

electron-deficient environment at the N site because W sites (using 5d valence orbital) is replaced by Ni using 3d valence orbital. From the N 1s spectra, W-N's binding energy in the NWN sample shifted by 0.27 eV compared to that of WN, indicating lower electron density around the N site in NWN compared to that of WN (Fig. 1e) [27]. The N 1s spectra of the WN sample showed two distinct peaks at 397.0 and 399.17 eV, assignable to W-N and N-H bonds, respectively [7]. The detection of the

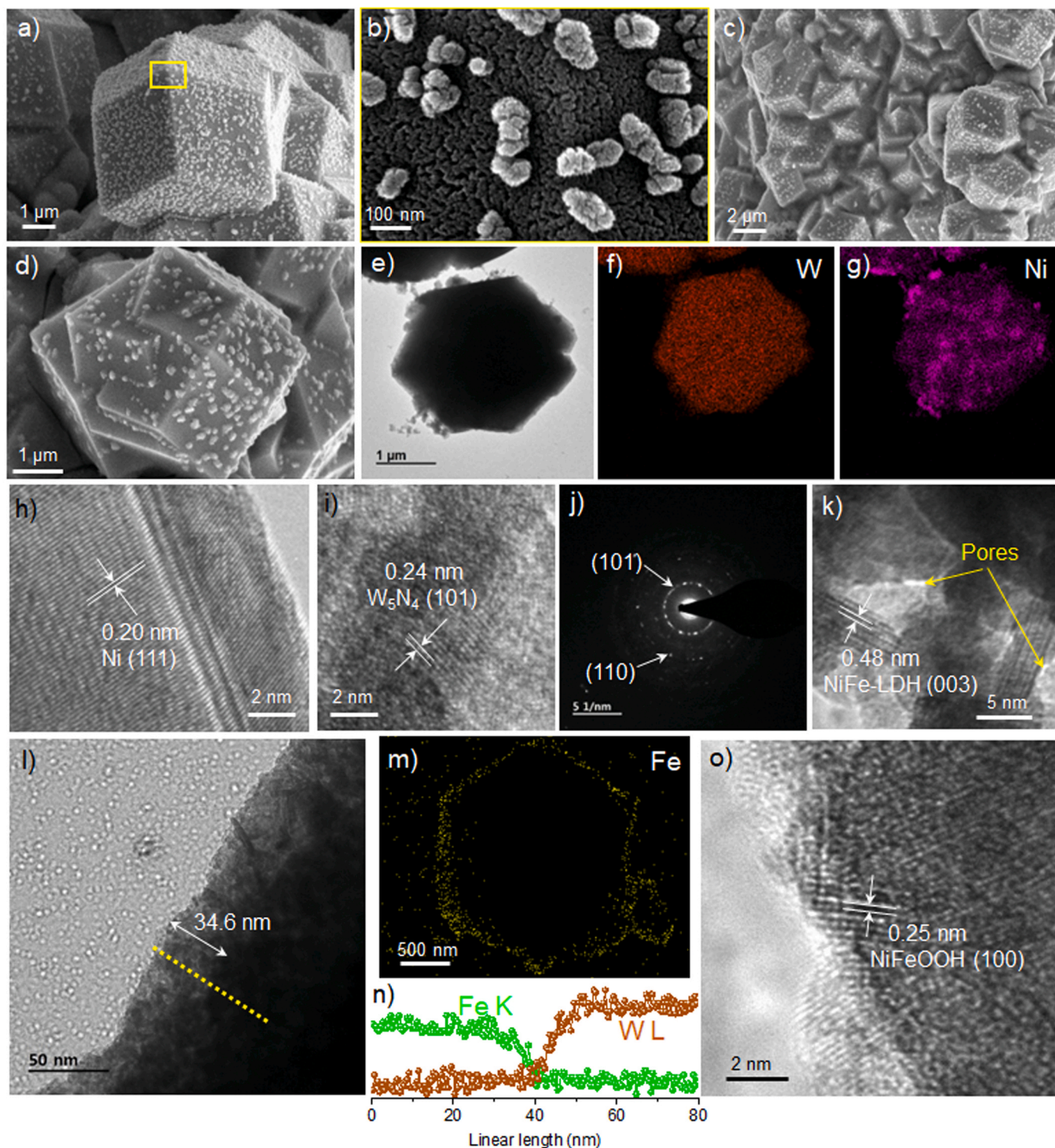


Fig. 2. HR-SEM images of a), b) NWN and c), d) NWN/NFO samples; e) HR-TEM image and f, g) elemental mapping of NWN electrode; h), i) high magnification HR-TEM images and j) SAED pattern of NWN electrode from diffraction plane analysis. HR-TEM image of k) NWN/NFO and l) NWN/NFO after ECR; m) elemental mapping and n) linear line mapping of NWN/NFO after ECR; o) high magnification HR-TEM image of the NWN/NFO after ECR.

N–H peak is due to a surficial N–H bond after the amination process; the small peak at 401.4 eV is related to the formation of an oxynitride bond (–ON) under air. The conformal coating of NFO over the NWN surface decreased the surface concentration of W and N elements (Table S2). Nonetheless, the dominance of the Ni^0 and W^0 peaks, even after NFO-coating procedure, indicated that a thin NFO layer had formed; however, electronic equilibrium between NWN and NFO caused the binding energy of the W–N peak in the NWN/NFO sample to shift. The O 1s spectrum of the NWN/NFO sample exhibited four major peaks at 529.83, 530.43, 531.06, and 532.28 eV, corresponding to metal oxide, oxygen vacancy (O_v), metal hydroxide, and adsorbed water, respectively (Fig. S2a). The Fe 2p spectrum of the NWN/NFO sample showed typical $2p_{3/2}$ and $2p_{1/2}$ spin-orbit couplings at 711.25 and 723.48 eV, respectively (Fig. S2b). The two major peaks at 710.81 and 712.45 eV represent the Fe^{2+} and Fe^{3+} states of the NFO co-catalyst [24,28].

Pristine WOH and WN samples have flower-like structures with well-aligned nanorod components (Fig. S3). Nanorod-like WN structures have widths of 40–50 nm and lengths of 200–300 nm. Incorporation of Ni into the WOH lattice induced a dramatic change in morphology. Small amounts of Ni-incorporation (Ni:W ratio = 0.75) agglomerated WOH nanorods into bundle form, and NWOH polyhedrons began to form (Fig. S4a–b). Increasing the Ni/W ratio (Ni:W ratio = 1.5, 3) formed hexagonal plate nanostructures, which merged with adjacent structures (Fig. S4c–f). By further increasing the Ni/W ratio (Ni:W ratio = 6, 9, and 12), hexagonal plates grew along the crystalline axis, forming polyhedrons (Fig. S4g–i). Those polyhedrons originated from initial positions on the hexagonal plates, but their shapes were random. The Ni:W ratio was optimized at 9:1 based on the HER results of the corresponding NWN sample (Fig. S5a). HR-SEM images of the optimized NWN sample are shown in Fig. 2a and b. The ammonia treatment made the polyhedron surface highly porous. A comparison of NWOH (Fig. S4k) and NWN (Fig. 2b) shows a dramatic increment of the surface porosity. Additionally, large nanoparticles formed on the surface due to extraction of Ni element; this was accompanied by the formation of W_5N_4 from $\text{Ni}_4\text{W}_6\text{O}_{21}(\text{OH})_2 \cdot 4\text{H}_2\text{O}$. The high-magnification HR-TEM image of these particles showed that the particles had porous structure similar to polyhedron (Fig. S6a). The energy dispersive X-ray spectroscopy (STEM-EDS) images show uniform distribution of W elements in the W_5N_4 lattice and a slightly random distribution of Ni elements overall in the polyhedrons (Fig. 2e–g). The STEM-EDS images of the particles showed the similar W and Ni distribution as a bulk polyhedron (Fig. S7). The NWN sample is identified as $\text{Ni}-\text{W}_5\text{N}_4$ alloy. The high magnification image of a single polyhedron indicates metallic Ni with a d -spacing of 0.20 nm, corresponding to the (111) plane (Fig. 2h). Another high magnification image from the bulk polyhedron shows a lattice distance of 0.24 nm, corresponding to the (101) plane of W_5N_4 (Fig. 2i) [19]. The selected area diffraction pattern (SAED) image of the polyhedron bulk shows distinct spots, indicating the high crystallinity of NWN. The major planes identified from the XRD analysis, including the (101), and (110) planes, are indexed in the SAED pattern (Fig. 2j).

The HR-SEM images of NWN/NFO sample show no differences from bare NWN, indicating that a very thin NFO co-catalyst layer was deposited on NWN (Fig. 2c, d). High magnification HR-TEM images of bare NWN and NWN/NFO are compared in Fig. S6b and c. The NWN/NFO sample shows distinct NFO nanoparticles over the NWN surface, with an average size of 5–10 nm. The high magnification image of the nanoparticles shows well-defined lattice fringes with d -spacing of 0.48 nm corresponding to the (003) plane of NiFe-LDH (Fig. 2k). The NFO nanoparticles layer was not continuous; however, after OER polarization (cyclic voltammogram, 0.0–0.5 V, 100 mV/s scan rate, 100 cycles), the high magnification HR-TEM image of the NWN/NFO shows that the NFO layer became continuous (Fig. 2l), having an average thickness of 20–40 nm, due to the formation of NiFeOOH through electrochemical reconstruction (ECR) of the NiFe-LDH pre-catalyst during the OER [29]. Linear line mapping (Fig. 2n), performed over the yellow line at the edge of NWN/NFO electrode (Fig. 2l), shows that a

distinct shell layer formed through the ECR. The STEM-EDS image of the NWN/NFO sample after ECR showed uniform distribution of Fe elements at the edges of the NWN polyhedrons (Fig. 2n). Interestingly, the high magnification image of NFO showed distinguishable lattice fringes with d -spacing of 0.25 nm corresponding to the (100) plane of $\gamma\text{-NiFeOOH}$ (Fig. 2o). [30] Therefore, the in situ formed NiFeOOH has crystalline nature. [31] The NFO layer thickness was optimized based on the OER yield of the corresponding NWN/NFO sample, as shown in Fig. S5b.

3.2. Electrocatalysis

Linear sweep voltammograms (LSV) of all electrode samples were obtained to evaluate the electrocatalytic activity and the LSV curves are presented after iR-compensation using the series resistance value measured by impedance spectroscopy. The current density obtained by electrocatalytic measurements was normalized using a geometric surface area of Ni foam 1 cm^2 . First, the hydrogen evolution reaction (HER) of the prepared electrode materials was examined. An NWN electrode sample showed higher catalytic activity at the lowest overpotential and a steeper increase of current density than those values of the WN, NWOH, and bare NF electrode samples (Fig. 3a and S8). The NWN electrode attained a current density of 10 mA/cm^2 at an overpotential of 10 mV (cf. 11 mV without iR-compensation), recording the best HER activity in the literature to date (Table S1). For comparison, LSV curves before iR-compensation are given in Fig. S9. The WN and NWOH electrodes exhibited relatively large overpotentials of 34 and 122 mV, respectively, at 10 mA/cm^2 . Furthermore, the mass activity of the NWN electrode sample (0.088 g/cm^2) was compared with a benchmark Pt/C (0.0055 g/cm^2) loaded on Ni foam (Fig. 3b). The NWN electrode showed more efficient HER half-cell activity than that of the Pt/C standard. Due to the intrinsic catalytic reactivity and the high conductivity, the NWN electrode reached a large current density of 1 A/cm^2 , requiring only an overpotential of 189 mV. The robustness and capability of the NWN electrode raise expectations of its potential for application in industrial H_2 production (see 3.4 section).

For an efficient Volmer–Tafel HER mechanism, abundant active sites at the interface can promote chemical desorption of H_2 product from adjacent H_{ads} groups. A low Tafel slope of 41.3 mV/dec was obtained with one NWN electrode sample, indicating that the HER follows the Volmer–Heyrovsky mechanism (Fig. 3c). Other electrode samples of WN (100.5 mV/dec) and NWOH (116.7 mV/dec) exhibited slightly larger Tafel slope values; these were ascribed to less efficient charge-transfer between active sites and H_{ads} . [32] Nonetheless, the similar Tafel slope values show that the HER with three electrodes follows the same reaction mechanism. Electrochemical active surface area (ECSA) of each electrode sample was calculated by obtaining the double-layer capacitance (C_{dl}) from the non-Faradic CV curve (Fig. S10). The WN electrode has a larger ECSA (373.3 cm^2) than those of the NWN (314.0 cm^2) and NWOH (148.5 cm^2) electrodes (Fig. 3d, Table S3). The large ECSA of the WN sample can be attributed to the well-defined flower-like architecture, very different from the bulk polyhedrons of the NWN sample. However, the HER activity trend of the three electrodes seems unrelated to the ECSA values. The ECSA value may falsely represent relative catalytic activity, unless catalyst samples belong to the same category [33]. The ECSA values of the nitride electrodes (WN, NWN), larger than those of their oxide counterparts (WOH, NWOH) are due to the increment of porosity after the thermal nitration procedure. The number of surface-active sites (N_A) is determined from the charge capacity of the electrode materials and obtained by integrating the reduction peak (Fig. S11). The NWOH, WN, and NWN electrodes have charge capacity values of 0.02, 0.039, and 0.045 C , respectively, giving values of N_A of 1.246×10^{17} , 2.447×10^{17} , and $2.830 \times 10^{17}\text{ cm}^{-2}$ for each electrode [34]. The trends of N_A value and specific activity (Fig. 3e) correspond to the I - V curves obtained with the three electrodes. These results show that surface composition needs to be modified to improve catalytic

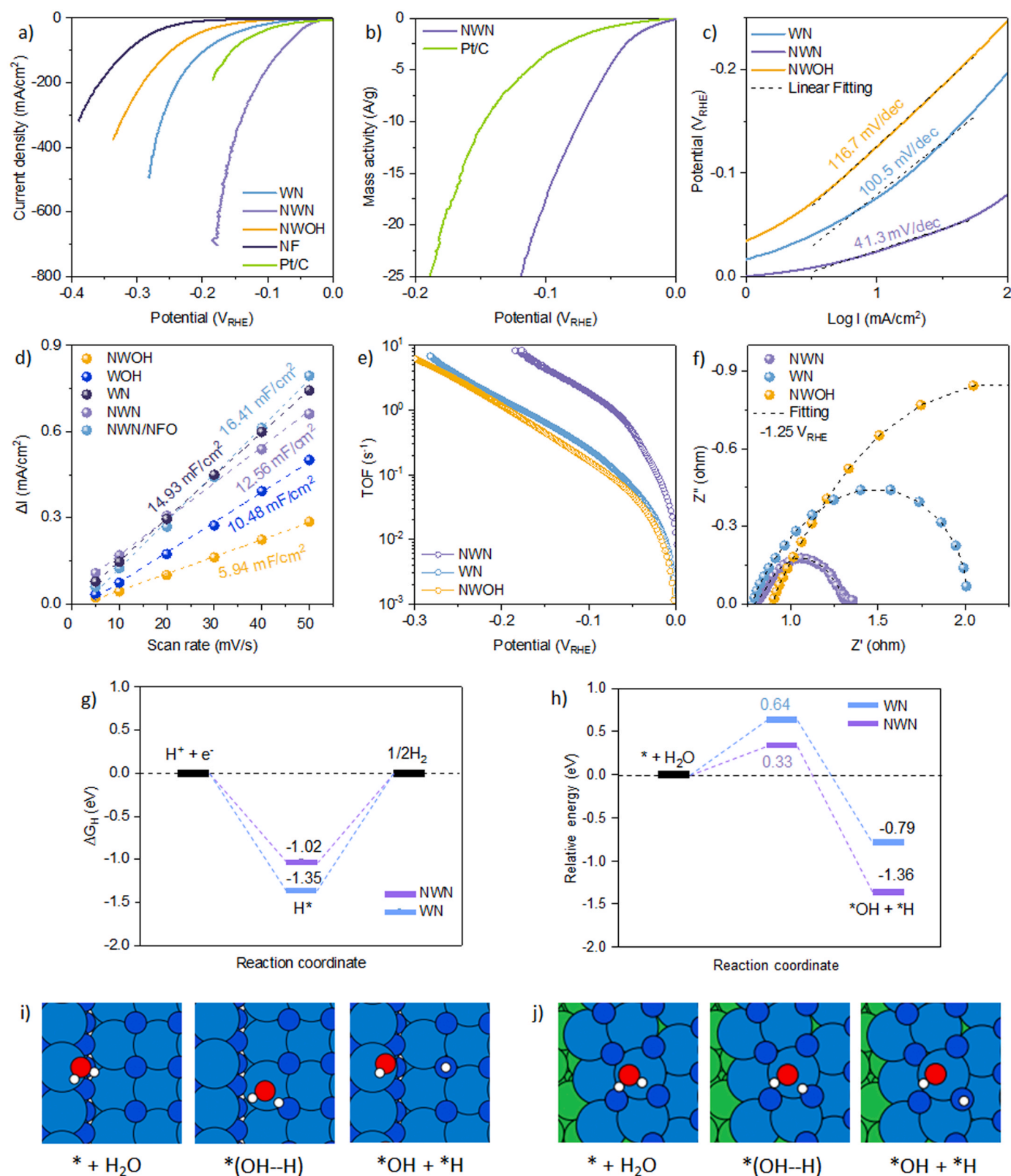


Fig. 3. a) LSV curves of electrode samples in HER half-cell, b) mass activity of NWN and Pt/C, c) Tafel plots, d) calculated ECSA values, e) compared TOF values of the prepared catalyst samples, and f) Nyquist plots, g) calculated H adsorption free energies on WN and NWN sample, h) calculated water dissociation activation energy for WN and NWN sample; schematic of water dissociation and adsorbed H formation on i) WN and j) NWN samples (blue: W, dark blue: N, green: Ni, red: O, white: H).

efficiency, rather than merely enlarging the ECSA value of the electrode surface.

Doping of second or third row transition metals (W, Mo, Pt, Ta, etc.) into first row transition metals is a common strategy to improve OER and HER efficiency because electronic modification of the *d* band structure can decrease energy barriers for formation or desorption of intermediates at active sites of first row transition metal-based catalysts [35–38]. However, the inverse case is rare, i.e., doping of first row metals into second or third row metals. Additionally, high-valence (>4+) transition metal ions have received relatively less attention in electrocatalytic applications. Recently, Nsanzimana et al. reported *d* band modification with a W–Ni alloy, in which W was proposed as an active site for proton reduction with an optimal free energy difference in the hydrogen adsorption step (ΔG_H) [39]. In the current synthetic approach, we alloyed Ni element with W_5Ni_4 ; the N site is likely a protonation site due to its strong nucleophilicity. [40,41] A reduction event of surficial W^{6+} to W^{4+} was detected with a reduction peak at 0.15 V in the LSV curve (Fig. S8). The XPS spectrum of the electrode sample after the HER experiment showed the high-valent states of W ions (Fig. S12a). H adsorption is strong at open-metal sites of Ni and W [42]; thus, N sites are expected to be active protonation sites. In a bare WN electrode, once the W^{4+} state is generated, electron density of N sites decreases and consequently decreases the HER reactivity of N sites. In contrast, in the case of an NWN electrode, metallic Ni donates electrons to N site oxidizing itself to $Ni^{2+/3+}$ as $Ni(OH)_2/Ni(O)OH$ species and subsequently making an electron-rich environment near N sites; this process enriches the electron density near the Fermi edge (see ultraviolet photoelectron spectroscopy (UPS) data in Fig. 5b). As shown in Fig. 3g, the ΔG_H of NWN is more thermoneutral than WN. The adsorption site changes from W site to N site after Ni alloying as shown in Fig. S13. The water dissociation activation energies on WN and NWN are 0.64 and

0.33 eV, respectively (Fig. 3h). The water dissociation activation energy of W site to form adsorbed H (Volmer step) reduced after Ni alloying, indicating that the kinetics of water dissociation is also accelerated by the Ni alloying. [43] Schematic of the water dissociation and the consecutive formation of adsorbed H on W site of WN and NWN is shown in Fig. 3i and j, respectively. The Nyquist plot obtained at -1.25 V shows that the metallic NWN electrode has a lower charge transfer resistance (R_{ct}) than those of the WN and NWOH electrodes, indicating that the potential drop across the NWN/electrolyte interface decreases with increased electron density (Fig. 3f).

Next, the oxygen evolution reaction (OER) of electrode samples was examined (Fig. 4a), and reverse LSV curves were used to determine overpotentials of electrodes without interference of oxidation peaks of metal ions. Unlike in the HER results, the OER activity of an NWN electrode was only slightly improved compared to that of a WN electrode. The Ni-alloying and morphology modification barely changed the reaction kinetics of the WN electrode in the OER half-cell. The catalytically active $Ni(O)OH$ species was generated after an ECR, and the Ni^{3+} state was detected with the NWN electrode after the OER experiment (Fig. S14). However, the OER kinetics of an NWN electrode looks slow, requiring an overpotential of 363 mV to attain 100 mA/cm^2 current density, which is only 23 mV lower than that of a WN electrode. To further enhance the sluggish OER, $NiFe(O)OH$ was incorporated into the NWN polyhedron surface; then, the overpotential at 100 mA/cm^2 decreased dramatically from 363 mV to 216 mV. Overpotentials (at 100 mA/cm^2) of the prepared electrode samples are compared in Fig. 4d; these values were obtained by changing the potential-scanning direction (forward and reverse LSV) and by performing reaction with/without iR-compensation. The LSV curves without iR-compensation are given in Fig. S15. The OER's catalytic parameters are compared with up-to-date reports in Table S1. The NWN/NFO electrode showed higher

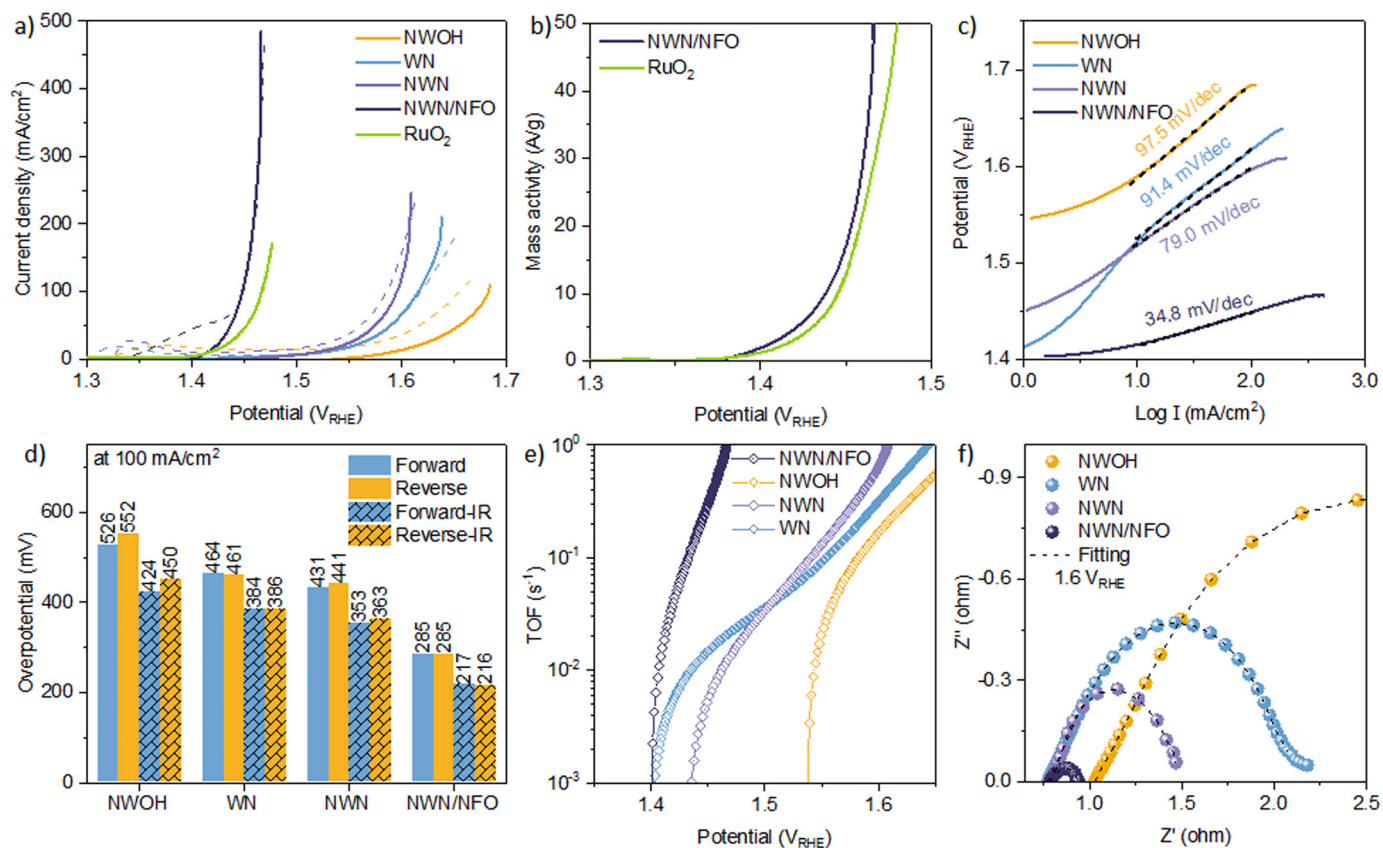


Fig. 4. a) LSV curves of electrode samples in OER half-cell (dotted line: forward scan, solid line: reverse scan), b) mass activity of NWN/NFO and RuO_2 standard, c) Tafel plots, d) comparison of overpotentials of the prepared catalyst samples at 100 mA/cm^2 , e) TOF values of electrode samples, and g) Nyquist plots.

activity than that of the RuO_2 standard in the OER half-cell reaction. The mass activity of the NWN/NFO electrode (0.0125 g/cm^2) was compared with benchmark RuO_2 (0.0055 g/cm^2) loaded on Ni foam (Fig. 4b). The NWN/NFO electrode attained a low Tafel slope of 34.8 mV/dec (Fig. 4c), but NWN (79.0 mV/dec) and WN (91.4 mV/dec) electrodes showed relatively large values. The Tafel slope decreased with incorporation of NFO co-catalyst, showing that W-neighboring Ni active sites cause a different rate determining step (RDS) from the case of Fe-neighboring Ni. For pristine NWN, formation of a hydroxyl intermediate ($\text{MO} + \text{OH}^- \rightarrow \text{MOOH} + \text{e}^-$) is the RDS at W-neighboring Ni active

sites because a large Tafel slope was obtained in the low overpotential region ($1.4 - 1.5 \text{ V}$). Deprotonation of MOH ($\text{MOH} + \text{OH}^- \rightarrow \text{MO} + \text{H}_2\text{O} + \text{e}^-$) is the RDS at Fe-neighboring Ni active sites.[44] The specific activity shown in Fig. 4e indicates that Fe-neighboring Ni active sites have more specific activity than W-neighboring Ni- or W- active sites. The high specific activity of the WN sample observed at only lower potential is due to morphological difference: there is a lower transport-limit when current density is small (Fig. 4c). The low Tafel slope of the NWN/NFO electrode can be attributed to fast charge-transfer kinetics at the electrode/electrolyte interface because NFO-incorporation generates more

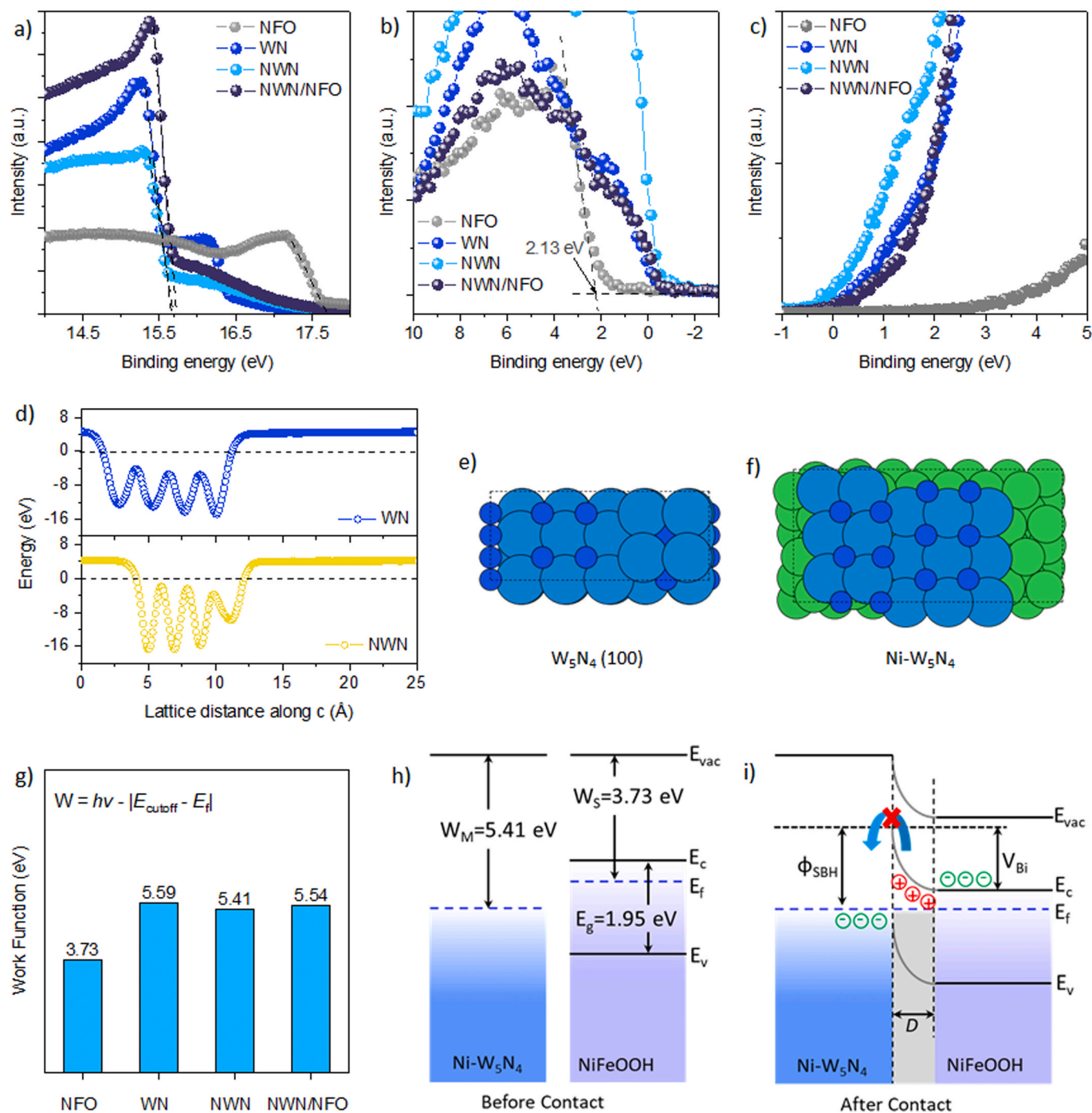


Fig. 5. UPS spectra in a) cutoff region and b) Fermi edge region, c) valance band XPS spectra, d) plane-averaged electrostatic potential along z-direction, e) slab structures of WN and NWN (blue: W, dark blue: N, green: Ni), g) calculated work function, h) band structures of NWN and NFO before contact, and i) formation of SJ between NWN and NFO.

active sites. Nyquist plots were obtained at 1.6 V to further examine the reaction kinetics at an electrode/electrolyte interface (Fig. 4f); the NWN/NFO electrode exhibited an R_{ct} value lower than those of the NWN, WN, and NWO electrodes, indicating that the NFO layer effectively enhances charge transfer.

3.3. Analysis of mechanism

The N_A values correlate to transferred electrons per unit

overpotential. The N_A of the NWN/NFO electrode is 2.78 times larger than that of the NWN sample; however, the NWN/NFO sample shows delayed onset potential and lower current density than those of the NWN electrode in the HER half-cell (Fig. S16). The inconsistent N_A -dependency of the HER and OER activity led us to focus on the NWN/NFO interface rather than the NFO/electrolyte interface. The physical property of the NWN/NFO junction was defined by valance band analysis using the XPS and UPS data. The cutoff energy (E_{cutoff}) values were derived by normalizing the secondary electron cutoff spectra (Fig. 5a).

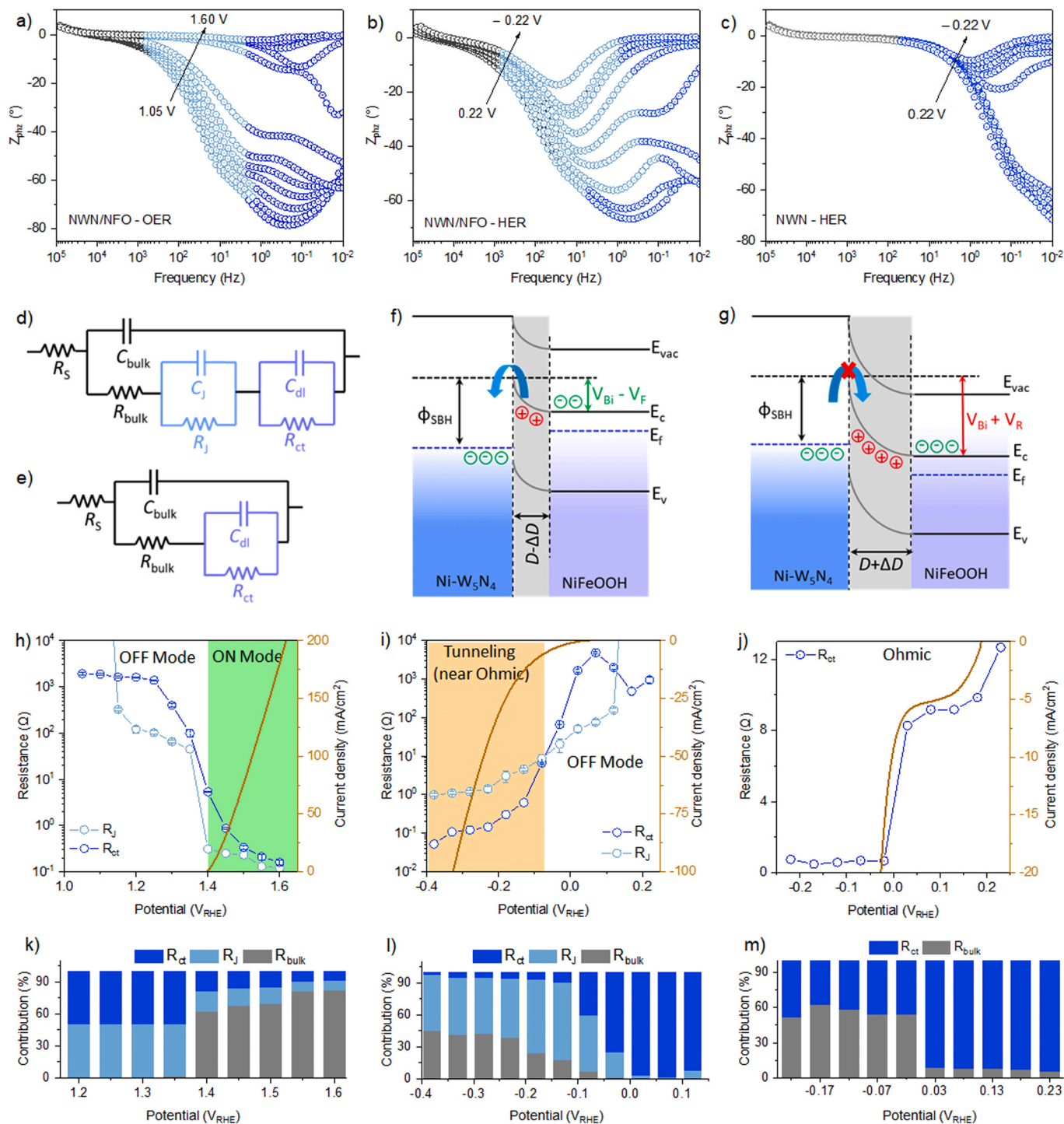


Fig. 6. Bode plots of NWN/NFO a) in OER half-cell and b) HER half-cell; c) Bode plot of NWN in HER half-cell; electronic circuits used to fit EIS spectra of d) NWN/NFO electrode and e) NWN electrode; band diagrams of NWN/NFO junction under f) forward bias and g) reverse bias; plots of junction resistance, charge-transfer resistance, and output current of h) NWN/NFO in OER half-cell and i) HER half-cell and j) NWN in HER half-cell; k)-m) contributions of individual resistances.

The work function (W) was calculated according to the following equation:[45].

$$W = h\nu - |E_{\text{cutoff}} - E_f|$$

where $h\nu$ is the energy of a photon and E_f is the Fermi edge. Fermi edge positions were obtained from the Fermi edge region as shown in Fig. 5b. As expected, both WN and NWN electrodes showed metallic behavior, whereas the NFO electrode exhibited a non-zero Fermi edge.[46] These properties were confirmed by the XPS valance band spectra (Fig. 5c). The obtained W values of the WN, NWN, NWN/NFO, and NFO electrodes were 5.59, 5.41, 5.54, and 3.73 eV, respectively (Fig. 5g). We also performed density functional theory calculations to verify the work function (W) and interpret the electronic property of the interface formed on the W_5N_4 (100) and Ni (111) surfaces (Fig. 5d-f). The work function was calculated as $W = E_{\text{vac}} - E_f$, where E_{vac} is the vacuum level energy. The DFT-calculated W values of W_5N_4 , Ni, and W_5N_4 /Ni heterostructures had similar trends with those obtained from the UPS analysis. The Mott–Schottky plot of the NFO electrode indicates n-type behavior (Fig. S17). The band gap (E_g) and position of the Fermi edge of the NFO electrode were determined from the Tauc plot (Fig. S18). The energy band diagram before contact is given in Fig. 5h. The NWN/NFO interface was identified as a rectifying unipolar Schottky diode consisting of metallic and semiconductor counterparts; it used electrons as a major carrier on both sides ($W_M > W_S$) [12]. Once electronic equilibrium was attained, a thin depletion layer formed at the NWN/NFO interface through extraction of free electrons from NFO to NWN. The depletion layer width (D) is dependent on the semiconductor doping level (Fig. 5i). Two important parameters, the Schottky barrier height (ϕ_{SBH}) and the built-in voltage barrier (V_{Bi}), determine the electron-flow across the SJ. ϕ_{SBH} is a constant value that regulates further flow of electrons across the junction in ‘off-mode’. However, external alteration of V_{Bi} (forward bias, $V_F > V_{\text{Bi}}$) can make electrons flow from semiconductor to metallic areas in ‘on-mode’. The on-mode increases electron-flow exponentially across the junction. Under forward bias condition (OER half-cell), V_{Bi} begins to decrease; there is also an accumulation of electrons at the conduction band (CB) of NFO. At higher bias, V_{Bi} disappears as allowing electrons flow from the CB of the NFO to NWN, which indicates disappearance of the depletion layer.

To confirm the mechanism, we measured the junction resistance (R_J) and capacitance (C_J) at various applied potentials using both forward and reverse polarizations. Direct electrochemical analysis of the solid-solid junction buried beneath the solid-electrolyte interface is difficult because of the dominance of the electrical double layer (EDL). We instead deployed EIS analysis to probe the real-time impact of the NWN/NFO junction on OER and HER half-cell reactions. Bode plots of the NWN/NFO electrode with forward and reverse polarization are shown in Fig. 6a and b, respectively; the three semicircles correspond to the bulk NWN ($10^5 - 10^3$ Hz, gray), the NWN/NFO junction ($10^3 - 10^0$ Hz, light blue), and the NFO/electrolyte interface ($10^0 - 10^{-2}$ Hz, blue). The plots were fitted using the electronic circuit shown in Fig. 6d [3,47]. Correlations among R_J , charge transfer resistance (R_{ct}), and current output under forward bias are shown in Fig. 6g. At a low forward bias ($V_F < 1.3$ V), there is no net current flow through the NFO/electrolyte interface and R_{ct} decreases in a linear fashion according to the applied bias; this behavior defines a typical n-type semiconductor/electrolyte interface. The R_J pattern shows three main regions of thinning of depletion layer ($V_F < 1.35$ V), breakdown of V_{Bi} (1.35 V $< V_F < 1.4$ V), and free flow of electrons ($V_F > 1.4$ V). At a low forward bias, electrons transferred from electrolyte to NFO accumulate at the depletion layer between NWN and NFO as the width of the depletion layer narrows. During this process, the CB of NFO shifts upward and V_{Bi} decreases. When V_F is equal to or higher than V_{Bi} , the depletion layer disappears, allowing electrons effortlessly to flow from the CB of the NFO to the NWN (thermionic emission) [15]. The onset potential of the OER current of the NWN/NFO electrode coincides exactly with the breakdown of V_{Bi} .

For the reverse bias (V_R , in a HER half-cell), the Bode plot also has three regions, similar to the case of the OER half-cell (Fig. 6b); however, dominant charge accumulation is observed at the NWN/NFO junction throughout the potentials applied (Fig. 6k). The applied reverse bias is in the same direction as that of V_{Bi} ; therefore, there is a continuous increment of V_{Bi} upon the reverse bias, which strongly resists electron flow across the NWN|NFO junction until a point of ‘reverse breakdown’. The reverse breakdown, known to permanently damage the SJ band structure by destroying its switching capability, allows electron-flow across the junction in both directions, typically demanding a few tens of volts of reverse bias. The current we observed in the reverse bias condition was due to electron tunneling from NWN to NFO. The off-mode achieved a ‘nearly ohmic’ condition in which an electron with a particular energy above the Fermi level of NWN can jump to a vacant site in the conduction band of NFO with the same energy level. This tunneling current depends on the doping density of the semiconductor and on the applied bias. However, the presence of tunneling current delays the HER onset significantly.

For comparison, a Bode plot of a pristine NWN electrode in an HER half-cell was obtained (Fig. 6c); it shows two semicircles corresponding to the bulk NWN ($10^5 - 10^1$ Hz, gray) and NWN/electrolyte ($10^1 - 10^{-2}$ Hz, blue) interfaces. The plots were fitted using the electronic circuit shown in Fig. 6e. The interface between the NWN/electrolyte is a metal|electrolyte junction; the R_{ct} value obtained before the HER onset was 1000 times smaller than that obtained at the NFO|electrolyte interface, which indicates the formation of a very thin EDL at the interface because metallic NWN electrode surface has abundant electron density. As shown in Fig. 6i, the correlation between the I - V curve and R_{ct} indicates that the HER on the NWN surface mainly depends on R_{ct} , whereas the HER on the NWN/NFO surface is dominated by R_J and remains almost constant even at high reverse bias. The point of reverse breakdown requires a higher reverse bias, which is the reason for the delay of the onset potential of the HER reaction compared to that of the bare NWN electrode. Contributions of R_J and R_{ct} to overall resistance ($R - R_s = R_{\text{bulk}} + R_{\text{ct}} + R_J$) are plotted against applied bias in Figs. 6j–6l. The value R_J plays a major role in the NWN/NFO electrode even at high HER potential; however, it becomes negligible at high OER potentials. Incorporation of unipolar SJ influenced the HER current even at high reverse bias; however, the catalytic activity in the HER half-cell was limited by the formation of SJ, even though ECSA and N_A values improved. Therefore, a unipolar SJ is not a proper setup for an HER half-cell or for other reductive reactions because additional overpotential is required. On the other hand, for an OER half-cell, proper band alignment using a metallic and semiconductor junction could reduce overpotential dramatically by efficient transfer of electrons from the semiconductor. The comparison of the specific activity of the NWN/NFO and NFO electrodes shows that the charge transport limits of the NFO catalyst are exceeded with the formation of SJ (Fig. S19). From the above discussions, we have given the design criteria of SJ for electrochemical interfaces in Table 1. The SJ can positively impact the electrochemical kinetics only under two configurations (green tick). The configurations with red ‘X’ mark will negatively impact the reaction kinetics. Therefore,

Table 1
Design criteria of Schottky junction for electrochemical interfaces.

Configuration	Reaction	$W_N > W_S$	$W_N < W_S$
Metal n-type	OER	✓	Ohmic
Metal n-type	HER	✗	Ohmic
Metal p-type	OER	Ohmic	✗
Metal p-type	HER	Ohmic	✓

the kinetics of HER can be increased by forming an SJ junction with a p-type metal/semiconductor configuration ($W_M < W_S$). Unfortunately, the best-known p-type semiconductors have a lower work function than WN and NWN. The ohmic behavior refers to the non-existence of SJ under those configurations. The Fermi level of metal and semiconductor are positioned in such a way that there is no depletion layer formation. Therefore, the current flow across the metal-semiconductor interface only depends on the applied potential irrespective of direction as per Ohm's law.

3.4. Durability of electrodes in seawater electrolyzer

Each NWN and NWN/NFO electrode exhibited outstanding catalytic performance in HER and OER half-cells, respectively. Thus, a two-electrode electrolyzer of NWN||NWN|NFO was assembled to assess the overall water splitting performance. A two-electrode cell set up with Sustainion X37-50 membrane was used as anion exchange membrane. Particularly, the durability of the prepared electrodes was examined under industrial operating conditions of high-temperature seawater. Seawater was collected from Black Sand Beach (Yeongseong-ri, South Korea) and filtered to remove fine sand particles and debris. Additionally, excess Mg and Ca ions in seawater were removed by forming less

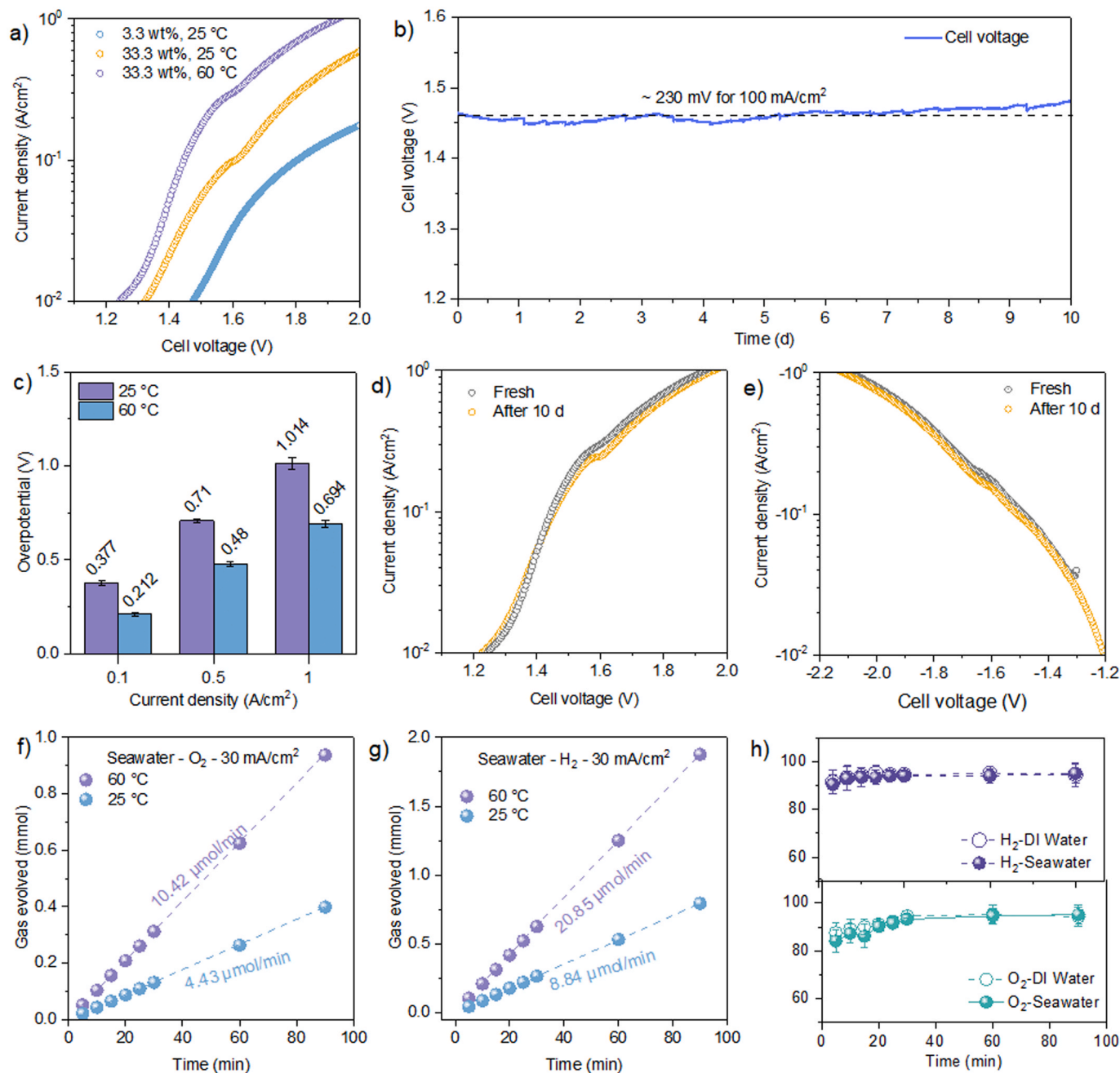


Fig. 7. a) LSV curves of an NWN||NWN|NFO electrolyzer under different operating conditions (without iR-compensation), b) chronoamperometry curves of the NWN||NWN|NFO electrolyzer maintained at 60 °C for 10 days, c) overpotentials required to attain different current densities, d)–e) LSV curves of the NWN||NWN|NFO electrolyzer before and after the 10 day-reaction under industrial conditions, f)–g) amounts of O_2 and H_2 gas measured at a current density of 100 mA/cm^2 in seawater electrolyte at 25 °C and 60 °C, and h) Faradaic efficiency of each HER and OER.

soluble $\text{Ca}(\text{OH})_2$ and $\text{Mg}(\text{OH})_2$ at high pH to avoid masking of electrode surface during electrolysis. [48,49] Fig. 7a shows LSV curves of NWN||NWN/NFO cell in the seawater electrolysis at two different $[\text{OH}^-]$ concentrations of 3.3 wt% KOH and 33.3 wt% KOH at 25 °C or 60 °C [50]. The results show the remarkable catalytic efficiency of the electrolyzer even for seawater containing various alkali/alkaline or halide ions. It is noteworthy that the electrolyzer required an overpotential of only 212 mV to attain 100 mA/cm^2 current density. The current density of 513 mA/cm^2 (without iR-compensation) was achieved at a potential less than 1.72 V, which is lower than the potential of hypochlorite formation. [51,52] Overpotentials of 0.21, 0.48, and 0.69 V were required to attain current density values of 100, 500, and 1000 mA/cm^2 (Fig. 7c), indicating even higher catalytic performance of this electrolyzer compared cases in the current literature (Table S4). In addition, the electrolyzer maintained its low overpotential without severe increase during continuous water splitting reaction over 10 days at a high current density of 100 mA/cm^2 (Fig. 7b). To rationalize the excellent performance and durability of the electrodes, the electrode surface after 10 day-seawater electrolysis was analyzed by phase, morphological and compositional analysis. HR-SEM images of the OER (NWN/NFO) and HER (NWN) electrodes are shown in Fig. S20a-c and d-f, respectively. The morphology of the NWN polyhedrons remained stable, while NWN/NFO polyhedrons deformed slightly after long-term electrolysis operation. HR-TEM images indicated that the OER and HER electrodes barely formed amorphous layer after a long-term electrolysis (Fig. S21). The XRD spectra showed crystalline peaks of the W_5N_4 phase after the electrolysis, indicating that both the OER and HER electrodes are not susceptible to degradation process such as corrosion, cation dissolution, or substrate detachment (Fig. S22). On the other hand, when a bare NWN was used as OER electrode, the polyhedron structure completely collapsed (Fig. S23), indicating that the NFO layer after ECR effectively prevents dissolution of W elements and increases chlorine corrosion resistance during seawater splitting reaction. Adsorption of inorganic chlorine (Cl^-) or insoluble Mg/Ca derivatives was not detected in the XPS analysis (Fig. S24 and Table S2). It seems that the minor deformation of NWN|NFO is related to only limited mass transfer at the electrode surface. The *I*-*V* curves obtained after the 10-day seawater splitting reaction show shapes similar to previous shapes (Fig. 7d, e), indicating shifts of overpotential of only 30 mV and 25 mV for OER and HER, respectively.

The amounts of H_2 and O_2 gases generated in the NWN||NWN/NFO electrolyzer were measured in both cases of using DI water and seawater electrolyte (Fig. S25). The O_2 gas evolution rate in seawater was 4.43 $\mu\text{mol}/\text{min}$, similar to the level in DI water (4.42 $\mu\text{mol}/\text{min}$), indicating the outstanding performance and durability of the NWN|NFO electrode in seawater electrolyte. The water splitting reactivity was further examined under industrial conditions of 100 mA/cm^2 and 60 °C (Fig. 7f, g). The gas evolution rates under the industrially favorable conditions were recorded at 20.85 and 10.42 $\mu\text{mol}/\text{min}$ for H_2 and O_2 gas; these values were almost three times higher those reported for seawater electrolysis at low temperature. The average Faradaic efficiency was above 95% in both DI water and seawater, indicating the highly selective reactivity of the NWN and NWN|NFO electrodes toward HER and OER, respectively (Fig. 7h).

4. Conclusion

A Schottky junction was constructed between metallic $\text{Ni-W}_5\text{N}_4$ and n-type NiFeOOH to overcome the conductance limit of (oxy)hydroxide OER active sites formed through ECR. The $\text{Ni-W}_5\text{N}_4/\text{NiFeOOH}$ electrode exhibited excellent catalytic activity toward OER, requiring small overpotentials of 216 at 100 mA/cm^2 and 233 mV at 500 mA/cm^2 . The dramatic increase of OER current is attributed to the rectifying Schottky junction, which accelerated electron-flow under forward polarization. Electrochemical analysis revealed that the current output is primarily affected by the Schottky junction rather than by the electrode/

electrolyte interface. The electrochemically active surface or the number of surface sites barely impacted the current output in the presence of the Schottky junction. The assembled electrolyzer with $\text{Ni-W}_5\text{N}_4||\text{Ni-W}_5\text{N}_4|\text{NiFeOOH}$ configuration was successfully demonstrated for industrial seawater electrolysis over a period of 10 days of continuous operation at 100 mA/cm^2 . The electrodes showed excellent durability and catalytic activity. Moreover, the design criteria and durable operation of the Schottky junction, proven in the OER/HER model studies, further highlight opportunities in various electrochemical energy conversion and storage systems.

CRedit authorship contribution statement

Selvaraj Seenivasan: Investigation, Writing – original draft. **Hyeonae Im:** Computing resource. **Taewael Lim:** Data curation. **Jeong Woo Han:** Computing resource, Supervision. **Junhyeok Seo:** Supervision, Funding acquisition, Writing – review & editing.

Declaration of Competing Interest

The authors declare that they have no known competing financial interests or personal relationships that could have appeared to influence the work reported in this paper.

Data availability

Data will be made available on request.

Acknowledgement

This work was supported by the National Research Foundation of Korea (NRF) grant funded by the Korea government (MSIT) (No. 2020R1C1C1007106 and 2021R1A5A1028138) and Korea Institute of Marine Science & Technology Promotion (KIMST) funded by the Ministry of Oceans and Fisheries, Korea (RS-2023-00224553).

Appendix A. Supporting information

Supplementary data associated with this article can be found in the online version at doi:10.1016/j.apcatb.2023.123233.

References

- [1] A. Gambhir, M. George, H. McJeon, N.W. Arnell, D. Bernie, S. Mittal, A.C. Köberle, J. Lowe, J. Rogelj, S. Monteith, Near-term transition and longer-term physical climate risks of greenhouse gas emissions pathways, *Nat. Clim. Change* (2021), <https://doi.org/10.1038/s41558-021-01236-x>.
- [2] Y. Dou, L. Sun, J. Ren, L. Dong, Chapter 10 - Opportunities and Future Challenges in Hydrogen Economy for Sustainable Development, in: A. Scipioni, A. Manzardo, J. Ren (Eds.) *Hydrogen Economy*, Academic Press 2017, pp. 277–305.
- [3] S. Seenivasan, H. Moon, D.-H. Kim, Multilayer strategy for photoelectrochemical hydrogen generation: new electrode architecture that alleviates multiple bottlenecks, *Nano-Micro Lett.* 14 (2022), 78, <https://doi.org/10.1007/s40820-022-00822-8>.
- [4] T. Grewe, M. Meggough, H. Tüysüz, Nanocatalysts for solar water splitting and a perspective on hydrogen economy, *Chem. – Asian J.* 11 (2016) 22–42, <https://doi.org/10.1002/asia.201500723>.
- [5] N.S. Lewis, D.G. Nocera, Powering the planet: Chemical challenges in solar energy utilization, *Proc. Natl. Acad. Sci.* 103 (2006) 15729–15735, <https://doi.org/10.1073/pnas.0603395103>.
- [6] Q. Wen, K. Yang, D. Huang, G. Cheng, X. Ai, Y. Liu, J. Fang, H. Li, L. Yu, T. Zhai, Schottky Heterojunction Nanosheet Array Achieving High-Current-Density Oxygen Evolution for Industrial Water Splitting Electrolyzers, *Adv. Energy Mater.* 11 (2021), 2102353, <https://doi.org/10.1002/aenm.202102353>.
- [7] S. Seenivasan, J. Seo, Inverting destructive electrochemical reconstruction of niobium nitride catalyst to construct highly efficient HER/OER catalyst, *Chem. Eng. J.* 454 (2023), 140558, <https://doi.org/10.1016/j.cej.2022.140558>.
- [8] W. Cai, R. Chen, H. Yang, H.B. Tao, H.-Y. Wang, J. Gao, W. Liu, S. Liu, S.-F. Hung, B. Liu, Amorphous versus crystalline in water oxidation catalysis: a case study of NiFe alloy, *Nano Lett.* 20 (2020) 4278–4285, <https://doi.org/10.1021/acs.nanolett.0c00840>.

- [9] S. Jin, Are metal chalcogenides, nitrides, and phosphides oxygen evolution catalysts or bifunctional catalysts? *ACS Energy Lett.* 2 (2017) 1937–1938, <https://doi.org/10.1021/acseenergylett.7b00679>.
- [10] Q. Zhou, L. Liao, H. Zhou, D. Li, D. Tang, F. Yu, Innovative strategies in design of transition metal-based catalysts for large-current-density alkaline water/seawater electrolysis, *Mater. Today Phys.* 26 (2022), 100727, <https://doi.org/10.1016/j.mtphys.2022.100727>.
- [11] J.-J. Lv, R. Yin, L. Zhou, J. Li, R. Kikas, T. Xu, Z.-J. Wang, H. Jin, X. Wang, S. Wang, Microenvironment Engineering for the Electrocatalytic CO₂ Reduction Reaction, *Angew. Chem. Int. Ed.* 61 (2022), e202207252, <https://doi.org/10.1002/anie.202207252>.
- [12] S. Seenivasan, K.I. Shim, C. Lim, T. Kavinkumar, A.T. Sivagurunathan, J.W. Han, D.-H. Kim, Boosting pseudocapacitive behavior of supercapattery electrodes by incorporating a schottky junction for ultrahigh energy density, *Nano-Micro Lett.* 15 (2023), 62, <https://doi.org/10.1007/s40820-023-01016-6>.
- [13] E.H. Rhoderick, Metal-semiconductor contacts, *IEEE Proc. I (Solid-State Electron Devices)* 14 (1) (1982).
- [14] K.K. Ng, Schottky-Barrier Diode, *Complet. Guide Semicond. Devices* (2009) 31–41.
- [15] C. Yim, N. McEvoy, H.-Y. Kim, E. Rezvani, G.S. Duesberg, Investigation of the interfaces in schottky diodes using equivalent circuit models, *ACS Appl. Mater. Interfaces* 5 (2013) 6951–6958, <https://doi.org/10.1021/am400963x>.
- [16] Z. Huang, H. Chen, X. He, W. Fang, W. Li, X. Du, X. Zeng, L. Zhao, Constructing a WC/NCN Schottky Junction for Rapid Electron Transfer and Enrichment for Highly Efficient Photocatalytic Hydrogen Evolution, *ACS Appl. Mater. Interfaces* 13 (2021) 46598–46607, <https://doi.org/10.1021/acsami.1c12063>.
- [17] X. Wang, X. Zong, B. Liu, G. Long, A. Wang, Z. Xu, R. Song, W. Ma, H. Wang, C. Li, Boosting Electrochemical Water Oxidation on NiFe (oxy) Hydroxides by Constructing Schottky Junction toward Water Electrolysis under Industrial Conditions, *Small*, n/a 2105544. <https://doi.org/https://doi.org/10.1002/smll.202105544>.
- [18] A. Kumar, V.Q. Bui, J. Lee, L. Wang, A.R. Jadhav, X. Liu, X. Shao, Y. Liu, J. Yu, Y. Hwang, H.T.D. Bui, S. Ajmal, M.G. Kim, S.-G. Kim, G.-S. Park, Y. Kawazoe, H. Lee, Moving beyond bimetallic-alloy to single-atom dimer atomic-interface for all-pH hydrogen evolution, *Nat. Commun.* 12 (2021), 6766, <https://doi.org/10.1038/s41467-021-27145-3>.
- [19] A.P. Wu, Y. Gu, B.R. Yang, H. Wu, H.J. Yan, Y.Q. Jiao, D.X. Wang, C.G. Tian, H. G. Fu, Porous cobalt/tungsten nitride polyhedra as efficient bifunctional electrocatalysts for overall water splitting, *J. Mater. Chem. A* 8 (2020) 22938–22946, <https://doi.org/10.1039/d0ta09620b>.
- [20] Y. Zhou, B. Chu, Z. Sun, L. Dong, F. Wang, B. Li, M. Fan, Z. Chen, Surface reconstruction and charge distribution enabling Ni/W5N4 Mott-Schottky heterojunction bifunctional electrocatalyst for efficient urea-assisted water electrolysis at a large current density, *Appl. Catal. B: Environ.* 323 (2023), 122168, <https://doi.org/10.1016/j.apcatb.2022.122168>.
- [21] Y. Duan, Z.-Y. Yu, L. Yang, L.-R. Zheng, C.-T. Zhang, X.-T. Yang, F.-Y. Gao, X.-L. Zhang, X. Yu, R. Liu, H.-H. Ding, C. Gu, X.-S. Zheng, L. Shi, J. Jiang, J.-F. Zhu, M.-R. Gao, S.-H. Yu, Bimetallic nickel-molybdenum/tungsten nanoalloys for high-efficiency hydrogen oxidation catalysis in alkaline electrolytes, *Nat. Commun.* 11 (2020), 4789, <https://doi.org/10.1038/s41467-020-18585-4>.
- [22] T. Wu, Z. Xu, X. Wang, M. Luo, Y. Xia, X. Zhang, J. Li, J. Liu, J. Wang, H.-L. Wang, F. Huang, Surface-confined self-reconstruction to sulfate-terminated ultrathin layers on NiMo3S4 toward biomass molecule electro-oxidation, *Appl. Catal. B: Environ.* 323 (2023), 122126, <https://doi.org/10.1016/j.apcatb.2022.122126>.
- [23] D. Wang, Q. Li, C. Han, Z. Xing, X. Yang, When NiO@Ni Meets WS₂ Nanosheet Array: A Highly Efficient and Ultrastable Electrocatalyst for Overall Water Splitting, *ACS Cent. Sci.* 4 (2018) 112–119, <https://doi.org/10.1021/acscentsci.7b00502>.
- [24] S. Seenivasan, S. Adhikari, D.-H. Kim, Surface restructuring of hematite photoanodes through ultrathin NiFeOx Catalyst: Amplified charge collection for solar water splitting and pollutant degradation, *Chem. Eng. J.* 422 (2021), 130137, <https://doi.org/10.1016/j.cej.2021.130137>.
- [25] S. Darmawi, S. Burkhardt, T. Leichtweiss, D.A. Weber, S. Wenzel, J. Janek, M. T. Elm, P.J. Klar, Correlation of electrochromic properties and oxidation states in nanocrystalline tungsten trioxide, *Phys. Chem. Chem. Phys.* 17 (2015) 15903–15911, <https://doi.org/10.1039/C5CP02482J>.
- [26] Z. Kang, H.-Y. He, R. Ding, J. Chen, B.C. Pan, Structures of WxNy crystals and their intrinsic properties: first-principles calculations, *Cryst. Growth Des.* 18 (2018) 2270–2278, <https://doi.org/10.1021/acs.cgd.7b01707>.
- [27] J. Baltrusaitis, P.M. Jayaweera, V.H. Grassian, XPS study of nitrogen dioxide adsorption on metal oxide particle surfaces under different environmental conditions, *Phys. Chem. Chem. Phys.* 11 (2009) 8295–8305, <https://doi.org/10.1039/B907584D>.
- [28] S. Selvaraj, H. Moon, J.-Y. Yun, D.-H. Kim, Iron oxide grown by low-temperature atomic layer deposition, *Korean J. Chem. Eng.* 33 (2016) 3516–3522, <https://doi.org/10.1007/s11814-016-0319-8>.
- [29] J. Zhang, J. Liu, L. Xi, Y. Yu, N. Chen, S. Sun, W. Wang, K.M. Lange, B. Zhang, Single-Atom Au/NiFe Layered Double Hydroxide Electrocatalyst: Probing the Origin of Activity for Oxygen Evolution Reaction, *J. Am. Chem. Soc.* 140 (2018) 3876–3879, <https://doi.org/10.1021/jacs.8b00752>.
- [30] Y. Wang, Y. Zhu, S. Zhao, S. She, F. Zhang, Y. Chen, T. Williams, T. Gengenbach, L. Zu, H. Mao, W. Zhou, Z. Shao, H. Wang, J. Tang, D. Zhao, C. Selomulya, Anion Etching for Accessing Rapid and Deep Self-Reconstruction of Precatalysts for Water Oxidation, *Matter* 3 (2020) 2124–2137, <https://doi.org/10.1016/j.matt.2020.09.016>.
- [31] P.W. Menezes, S. Yao, R. Beltrán-Suito, J.N. Hausmann, P.V. Menezes, M. Driess, Facile Access to an Active γ -NiOOH Electrocatalyst for Durable Water Oxidation Derived From an Intermetallic Nickel Germanide Precursor, *Angew. Chem. Int. Ed.* 60 (2021) 4640–4647, <https://doi.org/10.1002/anie.202014331>.
- [32] D. Navadeepthy, A. Rebekah, C. Viswanthan, N. Ponpandian, Boosting the kinetics of oxygen and hydrogen evolution in alkaline water splitting using nickel ferrite /N-graphene nanocomposite as a bifunctional electrocatalyst, *Int. J. Hydrog. Energy* 46 (2021) 21512–21524, <https://doi.org/10.1016/j.ijhydene.2021.03.244>.
- [33] S. Seenivasan, H. Jung, J.W. Han, D.-H. Kim, Surface roughening strategy for highly efficient bifunctional electrocatalyst: combination of atomic layer deposition and anion exchange reaction, *Small Methods* 6 (2022), 2101308, <https://doi.org/10.1002/smt.202101308>.
- [34] K. Karthick, S. Anantharaj, P.E. Karthik, B. Subramanian, S. Kundu, Self-assembled molecular hybrids of CoS-DNA for enhanced water oxidation with low cobalt content, *Inorg. Chem.* 56 (2017) 6734–6745, <https://doi.org/10.1021/acs.inorgchem.7b00855>.
- [35] C. Meng, T. Ling, T.-Y. Ma, H. Wang, Z. Hu, Y. Zhou, J. Mao, X.-W. Du, M. Jaroniec, S.-Z. Qiao, Atomically and electronically coupled Pt and CoO hybrid nanocatalysts for enhanced electrocatalytic performance, *Adv. Mater.* 29 (2017) 1604607, <https://doi.org/10.1002/adma.201604607>.
- [36] B. Zhang, X. Zheng, O. Voznyy, R. Comin, M. Bajdich, M. García-Melchor, L. Han, J. Xu, M. Liu, L. Zheng, F.P.Gd Arquer, C.T. Dinh, F. Fan, M. Yuan, E. Yassitepe, N. Chen, T. Regier, P. Liu, Y. Li, P.D. Luna, A. Janmohamed, H.L. Xin, H. Yang, A. Vojvodic, E.H. Sargent, Homogeneously dispersed multimetal oxygen-evolving catalysts, *Science* 352 (2016) 333–337, <https://doi.org/10.1126/science.aaf1525>.
- [37] B. Zhang, L. Wang, Z. Cao, S.M. Kozlov, F.P. García de Arquer, C.T. Dinh, J. Li, Z. Wang, X. Zheng, L. Zhang, Y. Wen, O. Voznyy, R. Comin, P. De Luna, T. Regier, W. Bi, E.E. Alp, C.-W. Pao, L. Zheng, Y. Hu, Y. Ji, Y. Li, Y. Zhang, L. Cavallo, H. Peng, E.H. Sargent, High-valence metals improve oxygen evolution reaction performance by modulating 3d metal oxidation cycle energetics, *Nat. Catal.* 3 (2020) 985–992, <https://doi.org/10.1038/s41929-020-00525-6>.
- [38] M. Gu, X. Deng, M. Lin, H. Wang, A. Gao, X. Huang, X. Zhang, Ultrathin NiCo bimetallic molybdate nanosheets coated CuOx nanotubes: heterostructure and bimetallic synergistic optimization of the active site for highly efficient overall water splitting, *Adv. Energy Mater.* 11 (2021), 2102361, <https://doi.org/10.1002/aenm.202102361>.
- [39] J.M.V. Nsanzimana, Y. Peng, M. Miao, V. Reddu, W. Zhang, H. Wang, B.Y. Xia, X. Wang, An Earth-Abundant Tungsten-Nickel Alloy Electrocatalyst for Superior Hydrogen Evolution, *ACS Appl. Nano Mater.* 1 (2018) 1228–1235, <https://doi.org/10.1021/acsnano.7b00383>.
- [40] J. Luo, X. Tian, J. Zeng, Y. Li, H. Song, S. Liao, Limitations and Improvement Strategies for Early-Transition-Metal Nitrides as Competitive Catalysts toward the Oxygen Reduction Reaction, *ACS Catal.* 6 (2016) 6165–6174, <https://doi.org/10.1021/acscatal.6b01618>.
- [41] H. Jin, H. Zhang, J. Chen, S. Mao, Z. Jiang, Y. Wang, A general synthetic approach for hexagonal phase tungsten nitride composites and their application in the hydrogen evolution reaction, *J. Mater. Chem. A* 6 (2018) 10967–10975, <https://doi.org/10.1039/C8TA02595A>.
- [42] S.H. Park, T.H. Jo, M.H. Lee, K. Kawashima, C.B. Mullins, H.-K. Lim, D.H. Yoon, Highly active and stable nickel-molybdenum nitride (Ni₂Mo₃N) electrocatalyst for hydrogen evolution, *J. Mater. Chem. A* 9 (2021) 4945–4951, <https://doi.org/10.1039/D0TA10090K>.
- [43] Y. Men, P. Li, J. Zhou, S. Chen, W. Luo, Trends in Alkaline Hydrogen Evolution Activity on Cobalt Phosphide Electrocatalysts Doped with Transition Metals, *Cell Rep. Phys. Sci.* 1 (2020), 100136, <https://doi.org/10.1016/j.xcrp.2020.100136>.
- [44] T. Shinagawa, A.T. Garcia-Esparza, K. Takanabe, Insight on Tafel slopes from a microkinetic analysis of aqueous electrocatalysis for energy conversion, *Sci. Rep.* 5 (2015), 13801, <https://doi.org/10.1038/srep13801>.
- [45] D. Liang, C. Lian, Q. Xu, M. Liu, H. Liu, H. Jiang, C. Li, Interfacial charge polarization in Co₂P₂O₇@N, P co-doped carbon nanocages as Mott-Schottky electrocatalysts for accelerating oxygen evolution reaction, *Appl. Catal. B: Environ.* 268 (2020), 118417, <https://doi.org/10.1016/j.apcatb.2019.118417>.
- [46] F. Ma, S. Wang, X. Gong, X. Liu, Z. Wang, P. Wang, Y. Liu, H. Cheng, Y. Dai, Z. Zheng, B. Huang, Highly efficient electrocatalytic hydrogen evolution coupled with upcycling of microplastics in seawater enabled by Ni₃N/W₅N₄ janus nanostructures, *Appl. Catal. B: Environ.* 307 (2022), 121198, <https://doi.org/10.1016/j.apcatb.2022.121198>.
- [47] W. Chen, B. Wu, Y. Wang, W. Zhou, Y. Li, T. Liu, C. Xie, L. Xu, S. Du, M. Song, D. Wang, Y. Liu, Y. Li, J. Liu, Y. Zou, R. Chen, C. Chen, J. Zheng, Y. Li, J. Chen, S. Wang, Deciphering the alternating synergy between interlayer Pt single-atom and NiFe layered double hydroxide for overall water splitting, *Energy Environ. Sci.* 14 (2021) 6428–6440, <https://doi.org/10.1039/D1EE01395E>.
- [48] Y. Sano, Y. Hao, F. Kuwahara, Development of an electrolysis based system to continuously recover magnesium from seawater, *Heliyon* 4 (2018), e00923, <https://doi.org/10.1016/j.heliyon.2018.e00923>.
- [49] C. Huang, Q. Zhou, L. Yu, D. Duan, T. Cao, S. Qiu, Z. Wang, J. Guo, Y. Xie, L. Li, Y. Yu, Functional Bimetal Co-Modification for Boosting Large-Current-Density Seawater Electrolysis by Inhibiting Adsorption of Chloride Ions, *Advanced Energy Materials*, n/a 2301475. <https://doi.org/https://doi.org/10.1002/aenm.202301475>.
- [50] C. Huang, Q. Zhou, D. Duan, L. Yu, W. Zhang, Z. Wang, J. Liu, B. Peng, P. An, J. Zhang, L. Li, J. Yu, Y. Yu, The rapid self-reconstruction of Fe-modified Ni hydroxysulfide for efficient and stable large-current-density water/seawater

- oxidation, *Energy Environ. Sci.* 15 (2022) 4647–4658, <https://doi.org/10.1039/D2EE01478E>.
- [51] C. Andronesco, S. Seisel, P. Wilde, S. Barwe, J. Masa, Y.-T. Chen, E. Ventosa, W. Schuhmann, Influence of temperature and electrolyte concentration on the structure and catalytic oxygen evolution activity of nickel–iron layered double hydroxide, *Chem. – A Eur. J.* 24 (2018) 13773–13777, <https://doi.org/10.1002/chem.201803165>.
- [52] G.-F. Li, M. Divinagracia, M.F. Labata, J.D. Ocon, P.-Y. Abel Chuang, Electrolyte-dependent oxygen evolution reactions in alkaline media: electrical double layer and interfacial interactions, *ACS Appl. Mater. Interfaces* 11 (2019) 33748–33758, <https://doi.org/10.1021/acsami.9b06889>.